Journal of Power Sources 195 (2010) 4297–4303

Contents lists available at ScienceDirect

Journal of Power Sources

journal homepage: www.elsevier.com/locate/jpowsour

Basic molten salt process—A new route for synthesis of nanocrystalline $Li_4Ti_5O_{12}$–TiO_2 anode material for Li-ion batteries using eutectic mixture of $LiNO_3$–LiOH–Li_2O_2

M.M. Rahman[a,*], Jia-Zhao Wang[a], Mohd Faiz Hassan[a,c], Shulei Chou[a], David Wexler[b], Hua-Kun Liu[a]

[a] Institute for Superconducting and Electronic Materials & ARC Centre of Excellence for Electromaterials Science, University of Wollongong, Northfields Ave, Wollongong, New South Wales 2522, Australia
[b] School of Mechanical, Materials and Mechatronic Engineering, University of Wollongong, Australia
[c] Department of Science Physics, University of Malaysia Terengganu, Kuala Terengganu 20522, Malaysia

ARTICLE INFO

Article history:
Received 21 October 2009
Received in revised form
30 December 2009
Accepted 21 January 2010
Available online 4 February 2010

Keywords:
Molten salt
Basic environment
$Li_4Ti_5O_{12}$–TiO_2 anode
Lithium-ion batteries

ABSTRACT

A nanocrystalline $Li_4Ti_5O_{12}$–TiO_2 duplex phase has been synthesized by a simple basic molten salt process (BMSP) using an eutectic mixture of $LiNO_3$–LiOH–Li_2O_2 at 400–500 °C. The microstructure and morphology of the $Li_4Ti_5O_{12}$–TiO_2 product are characterized by means of X-ray diffraction (XRD), field emission scanning electron microscopy (FE-SEM), and transmission electron microscopy (TEM). The sample prepared by heat-treating at 300 °C for 3 h (S-1) reveals dense agglomerates of ultra-fine nanocrystalline $Li_4Ti_5O_{12}$; with heat treatment at 400 °C for 3 h (S-2), there is a duplex crystallite size (fine < 10 nm, and coarse > 20 nm) of $Li_4Ti_5O_{12}$–TiO_2; at 500 °C for 3 h (S-3), a much coarser and less-dense distribution of lithium titanate (crystallite size ~15–30 nm) is observed. According to the results of electrochemical testing, the S-2 sample shows initial discharge capacities of 193 mAh g^{-1} at 0.2 C, 168 mAh g^{-1} at 0.5 C, 146 mAh g^{-1} at 1 C, 135 mAh g^{-1} at 2 C, and 117 mAh g^{-1} at 5 C. After 100 cycles, the discharge capacity is 138 mAh g^{-1} at 1 C with a capacity retention of 95%. The S-2 sample yields the best electrochemical performance in terms of charge–discharge capacity and rate capability compared with other samples. Its superior electrochemical performance can be mainly attributed to the duplex crystallite structure, composed of fine (<10 nm) and coarse (>20) nm nanoparticles, where lithium ions can be stored within the grain boundary interfaces between the spinel $Li_4Ti_5O_{12}$ and the anatase TiO_2.

1. Introduction

Lithium-ion batteries are considered to be the most promising energy-storage technology for hybrid, plug-in hybrid, and all-electric vehicle applications [1]. The capacity of the batteries at high discharge rates is critically dependent not only on the morphology of the battery active materials and the microstructure of the electrode, but also on the Li^+ diffusion coefficient in the solid electrode material [2,3]. State-of-the-art lithium secondary batteries have graphite/carbon-related negative electrodes (anodes) [4,5], which cause serious safety concerns for large-size applications. Due to the low lithium intercalating voltage of approximately 100 mV (vs. Li/Li^+), highly reactive metallic lithium forms easily under a fast charge rate, and this lithium will be deposited on the surface of the electrode particles to create a high risk of reaction with the electrolyte or with a highly-charged cathode [6].

Much interest has focused on the development of new electrode materials that exhibit higher capacities, lower cost, environmental friendliness, and increased safety [7]. Li-titanate and various TiO_2-polymorph based cells are safer because these materials are chemically compatible with the electrolyte and the total specific energy of the cell is much lower. The voltages of Li-titanate and TiO_2 electrodes are significantly higher and the capacities are significantly lower than those of the graphite-based Li-ion cells. Because of such considerations, these oxide anodes could be considered as complementary to carbonaceous anodes in Li-ion batteries.

Interest in titanium oxide materials for anode applications can be traced back to the observation of Li-insertion activities in the lithium titanates. Since the early 1990s, Dahn and co-workers [8], Thackeray and co-workers [9] and Ohzuku et al. [10] have reported the Li-insertion properties of spinel oxides $Li_{1+x}Ti_{2-x}O_4$, $0 \le x \le 1/3$. Both metallic $LiTi_2O_4$ and semiconducting $Li_{4/3}Ti_{5/3}O_4$ ($Li_4Ti_5O_{12}$) exhibit similar Li-insertion electrochemistry; the Li insertion potential is 1.36–1.338 V for $LiTi_2O_4$ [8,11].

* Corresponding author. Tel.: +61 2 4298 1478; fax: +61 2 4221 5731.
E-mail addresses: mmr543@uow.edu.au, mokhles_utm@yahoo.com (M.M. Rahman).

0378-7753/$ – see front matter © 2010 Elsevier B.V. All rights reserved.
doi:10.1016/j.jpowsour.2010.01.073

It has been reported [10] that electrochemical intercalation and deintercalation of lithium is quite reversible in lithium titanate ($Li_{4/3}Ti_{5/3}O_4 + Li^+ + e^- \leftrightarrow Li_{7/3}Ti_{5/3}O_4$), although the electrode potential is ~1.5 V relative to Li/Li$^+$, which is higher than that of lithium-intercalated graphite. Spinel $Li_4Ti_5O_{12}$ is a so-called zero-strain insertion material as the anode material of lithium secondary batteries [10]. Since $Li_4Ti_5O_{12}$ does not act as a Li^+ source, this material can, in principle, be coupled with high voltage cathodes such as $LiMn_2O_4$, $LiNiO_2$ or $Li_2CoMn_3O_8$ to produce a cell with an operating voltage of approximately 2.5 V and with high safety and reversibility [12–14]. One of the most important properties of $Li_4Ti_5O_{12}$ is that its lattice parameters are almost unchanged when lithium ions are inserted and extracted. The material accommodates Li to a theoretical capacity of 175 mAh g^{-1}; the actual discharge capacity is >160 mAh g^{-1} [15]. On the other hand, titanium oxide (anatase) has been found to be one of the best candidates as a host for lithium ions because it is a fast Li insertion/extraction host with a high theoretical capacity of 336 mAh g^{-1}, and has the added advantages of low cost, nontoxicity, an appropriate insertion potential (~2.0 V), low volume expansion (3–4%) during lithium insertion [16], and environmental friendliness [17]. The reversible lithium insertion coefficient x (Li_xTiO_2) may depend on the crystallography and microstructure of the materials; it has a value of up to 0.5 mol Li per mol TiO_2 [18,19] at room temperature.

In most previous studies, spinel $Li_4Ti_5O_{12}$ has been synthesized by means of a solid-state reaction with heating at 800–1000 °C for 12–24 h [8,20–23] or the sol–gel method [24–27]. The conventional solid-state reaction requires high-temperature heating for a long time, and the product exhibits inhomogeneity, irregular morphology, and a broad particle-size distribution [28–31]. Nanosized spinel $Li_4Ti_5O_{12}$ with a high specific surface area of 100 m^2 g^{-1} has been prepared via a sol–gel route and found to have an excellent high-rate performance, even at a charging rate as high as 250 C [32]. Although the sol–gel method offers some advantages, the difficult synthesis conditions and the requirement for a large quantity of solvents and organic materials, such as citric acid, ethylene glycol and polyvinyl alcohol, present bottlenecks with respect to large-scale manufacture [33].

At present, the mass production of extremely small-sized electrode materials, especially with particle sizes of 10 nm or smaller, has yet to be realized [34–36]. Synthesis in low-temperature inorganic molten salts is one potential process for this purpose; in particular, for the synthesis of intercalation oxide electrode materials such as $LiCoO_2$, $LiMn_2O_4$, and other compounds [37–40]. Nevertheless, there have been few reports of the synthesis of $Li_4Ti_5O_{12}$ anode material by the molten salt process. This study examines the synthesis of $Li_4Ti_5O_{12}$–TiO_2 anode material by a low temperature, basic molten salt precipitation route, which is a method that is quite different to others reported in the literature. Thus, it is very interesting to explore the synthesis of $Li_4Ti_5O_{12}$–TiO_2 nanoparticles by the basic molten salt process and their application as alternative anodes to carbonaceous materials in Li-ion batteries.

2. Experimental

2.1. Materials synthesis

The precursors of $Li_4Ti_5O_{12}$ powder samples were synthesized using $LiNO_3$ (Sigma–Aldrich, 99.9%), $LiOH{\cdot}H_2O$ (Sigma–Aldrich, 98%), Li_2O_2 (Sigma–Aldrich, 90%), and $Ti[O(CH_2)_3CH_3]_4$ (Sigma–Aldrich, 97%) as starting materials. The molar ratio of the eutectic mixture of $LiNO_3$:$LiOH{\cdot}H_2O$:Li_2O_2 was fixed at 0.05:0.1:0.1. The compounds were mixed thoroughly and ground in a mortar with a pestle. $Ti[O(CH_2)_3CH_3]_4$ (0.5 mol) was added to the mixture dropwise with further guiding to form a homogeneous slurry. The powder mixture was vacuum dried at 120 °C for 24 h. The drying process was used to minimize the water content in the starting material mixture for the molten salt ($LiNO_3$–$LiOH{\cdot}H_2O$). The mixture was immediately transferred to a muffle furnace and calcined at 300 °C for 3 h (S-1), 400 °C for 3 h (S-2), and 500 °C for 3 h (S-3). The heating rate was 10 °C min^{-1} for all temperature settings. The $LiNO_3$–$LiOH{\cdot}H_2O$–Li_2O_2 mixture became a molten salt near the eutectic composition. This was significantly different from an aqueous solution, and the water content of the molten salt solution was reduced as much as possible. The solution thus became very basic, which led to the production of stable $Li_4Ti_5O_{12}$ and $Li_4Ti_5O_{12}$–TiO_2 phases. In addition, the effects of Li_2O_2 may both increase the basicity and also accelerate in situ oxidation within the molten salts. A black powder was immediately precipitated in the molten salt solution. After cooling and solidification, this solid mixture was immersed in de-ionized water, and all of the salt elements were dissolved. The precipitated black powders, which are the metal oxide particles, are insoluble in water, so that all of the precipitates could be separated. The resultant particles were collected and vacuum treated again at 120 °C for 24 h to eliminate residual water on the particle surfaces. The dried powders were then subjected to structural characterization and electrochemical measurements.

2.2. Composition and structure determination

X-ray diffraction (XRD) data were collected from powder samples on a Philips PW1730 diffractometer (with Cu Kα radiation, λ = 1.54056 Å, and a graphite monochromator) at a scanning rate of 2° min^{-1} for 2θ in the range of 10–90°. Traces^{TM} software in combination with the Joint Committee on Powder Diffraction Standards (JCPDS) powder diffraction files was used to identify the phases present. The Brunauer–Emmet–Teller (BET) surface areas of the synthesized materials were measured by a NOVA 1000 high-speed gas sorption analyzer (Quantachrome Corporation, USA). The morphologies of the samples were investigated by transmission electron microscopy (TEM) using a JEOL 2011 analytical electron microscope. TEM samples were prepared by deposition of ground particles on lacey carbon support films.

2.3. Electrode preparation, coin cell assembly, and electrochemical measurements

To test their electrochemical performance, the $Li_4Ti_5O_{12}$ and $Li_4Ti_5O_{12}$–TiO_2 nanomaterials were mixed with acetylene black (AB) (Cabot Australasia Pty Ltd.) and a binder, polyvinylidene fluoride (PVdF, Sigma–Aldrich), in a weight ratio of 80:10:10 in a solvent, *N*-methyl-2-pyrrolidone (NMP, Sigma–Aldrich, anhydrous, 99.5%). The slurry was uniformly spread on copper foil substrates, each with an area of 1 cm^2. The coated electrodes (average thickness ~50 μm) were dried in a vacuum oven at 100 °C for 24 h and then pressed under a pressure for 10 s. Subsequently, the electrodes were cut to a 1 × 1 cm^2 size, and CR 2032 coin-type cells were assembled in an argon-filled glove-box (Mbraun, Unilab, Germany). The electrochemical coin cells contained a coated electrode on copper foil as the working electrode, lithium foil as the counter electrode and the reference electrode, porous polypropylene as the separator, and 1 M LiPF6 in a 50:50 (v/v) mixture of ethylene carbonate and dimethyl carbonate (MERCK KgaA, Germany) as the electrolyte. Charge–discharge and cyclic voltammetry (CV) measurements were performed using a Neware battery test station and a CHI 660b electrochemistry workstation, respectively. The cells were galvanostatically discharged and charged in the range of 1.0–2.5 V at different current densities. Cyclic voltammet-

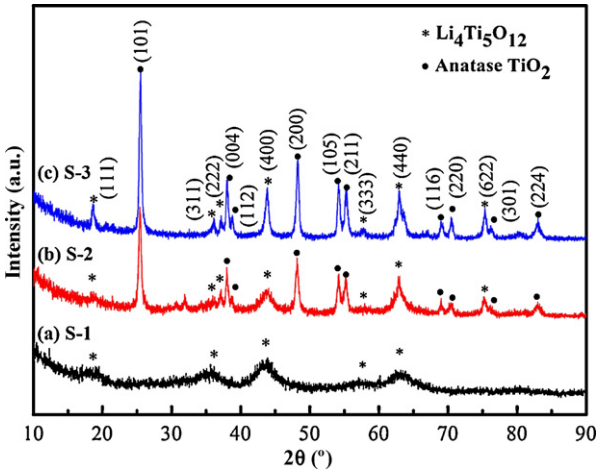

Fig. 1. X-ray diffraction patterns of S-1, S-2 and S-3 samples synthesized at (a) 300 °C, (b) 400 °C and (c) 500 °C.

ric measurements of the electrodes were performed at a scan rate of 0.05 mV s^{-1} between 1.0 and 2.5 V vs. Li/Li^+.

3. Results and discussion

The structures and phases present in the synthesized compounds were investigated by X-ray diffraction (XRD). The results for samples S-1 (a), S-2 (b) and S-3 (c) – calcined at 300, 400, and 500 °C, respectively – are shown in Fig. 1. In all samples, diffraction peaks consistent with the cubic spinel phase, $Li_4Ti_5O_{12}$ [space group Fd-3m (2 2 7), JCPDS No. 49-0207], are observed; the individual sets of planes are indexed in the figure. Additional narrow peaks are observed. These are consistent with the presence of TiO_2 anatase [space group: 141/amd (1 4 1), JCPDS No. 89-4921] and are also indexed in Fig. 1. Sample S-1 (calcined at 300 °C for 3 h) contained the pure phase $Li_4Ti_5O_{12}$; no other impurity peaks are detected. The peaks associated with $Li_4Ti_5O_{12}$ are significantly broadened, particularly for samples calcined at 300 and 400 °C. This feature is consistent with the formation of lithium titanate nanocrystals of increasing nanocrystallite size in the order of increasing calcination temperature. The approximate crystallite sizes of the $Li_4Ti_5O_{12}$ and $Li_4Ti_5O_{12}$–TiO_2 phases in the powders were estimated using the Debye–Scherrer equation applied to the marked peaks, which are assumed to originate from (4 0 0) $Li_4Ti_5O_{12}$, where the Si standard 2 2 0 peak is used as the full-width half-maximum (FWHM) reference (0.204°) for the unbroadened peak. The results are listed in Table 1.

Table 1
Specific surface areas and crystal sizes of S-1, S-2 and S-3 samples.

Samples	S-1	S-2	S-3
Treatment time (h)	3	3	3
Crystallite sizes (nm)	1.9	5.1	25.8
BET ($m^2\ g^{-1}$)	110.92	76.43	28.53

The specific surface areas of the synthesized products were measured by the 15 BET N_2 adsorption method and are shown in Table 1. Sample S-1 shows the highest specific surface area (110.92 $m^2\ g^{-1}$), while samples S-2 and S-3 report values of 76.43 and 28.53 $m^2\ g^{-1}$, respectively. Thus, the surface areas follow the trend of 300 °C (S-1) > 400 °C (S-2) > 500 °C (S-3), i.e., smaller crystal sizes are associated with higher surface areas. In summary, the results indicate that pure $Li_4Ti_5O_{12}$ phase with very small crystal size can be synthesized at a very low temperature by the basic molten salt process whereas, with increasing temperature, there is a significant possibility that anatase TiO_2 will be formed as a secondary phase.

Preliminary TEM investigations reveal additional information concerning structural and morphological evolution as a function of synthesis temperature. Bright-field imaging of the sample prepared at 300 °C (Fig. 2(a)–(c)) reveals dense agglomerates of ultra-fine nanocrystalline $Li_4Ti_5O_{12}$, with associated selected area electron diffraction (SAED) patterns containing very diffuse rings (inset to Fig. 2(a)), while high-magnification imaging indicates crystallite sizes between about 2 and 5 nm (Fig. 2(c)). A much coarser and less-dense distribution of lithium titanate (crystallite size ~15–30 nm) is observed in the sample prepared at 500 °C. Thus the sample can be described as mesoporous. In addition to the SAED spotty rings

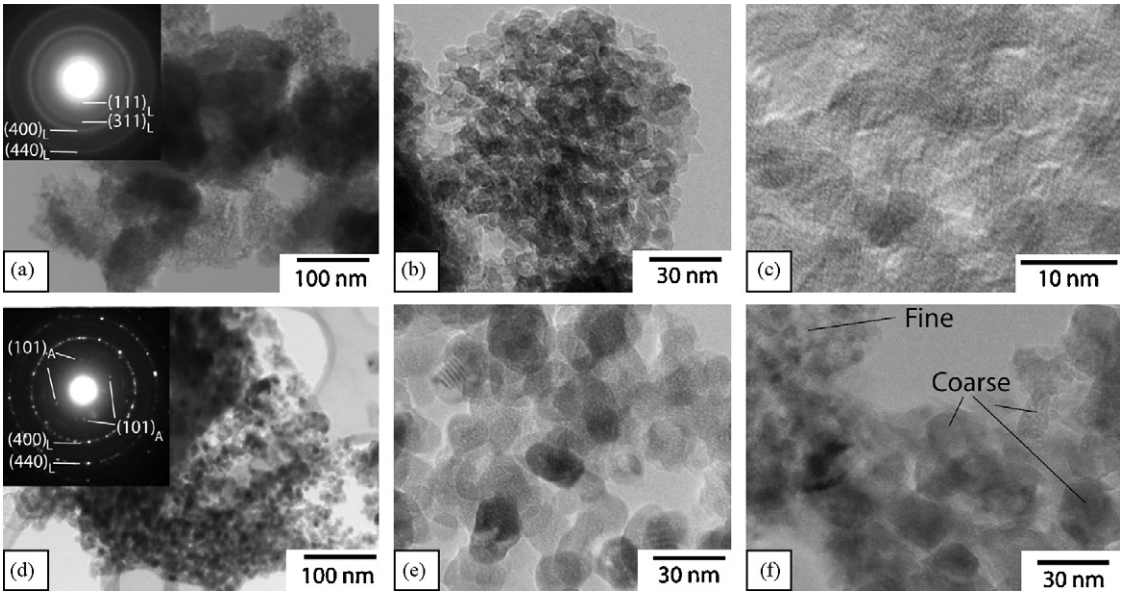

Fig. 2. TEM bright-field images and corresponding SAED patterns (insets) revealing differences in samples prepared at 300 °C ((a)–(c)), 500 °C ((d) and (e)), and 400 °C (f). Diffuse rings in SAED pattern associated with region (a) are indexed as nanocrystalline $Li_4Ti_5O_{12}$ (subscripted L), while high-magnification image (c) indicates a crystallite size of ~2–5 nm. Spotty rings in SAED pattern in (d) are consistent with much coarser $Li_4Ti_5O_{12}$ obtained at higher temperature (~15–25 nm particle size according to (e)), with additional reflections present and interplanar spacings consistent with anatase phase (subscripted A). In sample synthesized at 400 °C (f), local regions of fine and coarse crystallites are observed, as indicated.

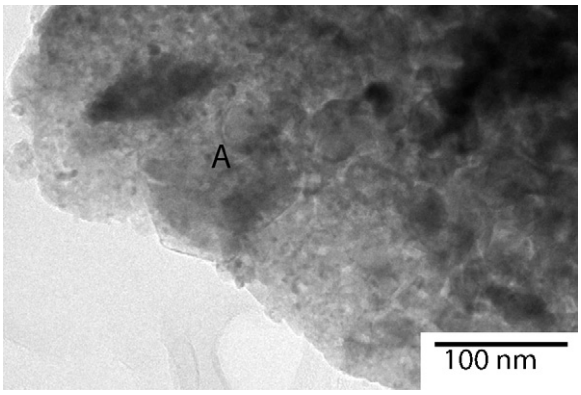

Fig. 3. TEM bright-field image indicating growth of large facetted crystals believed to consist of anatase phase (marked A) in a predominately lithium titanate nanostructure (Sample S-3).

associated with $Li_4Ti_5O_{12}$, additional SAED spots provided evidence of the presence of anatase TiO_2 phase (compare Fig. 2(a) and (d)). In the sample prepared at 400 °C, a duplex lithium titanate crystallite size is observed, as indicated by the regions of fine (<10 nm) and coarse (>20 nm) nanoparticles, as marked in Fig. 2(f). Additional large facetted crystals, believed to consist of anatase, are observed at the higher synthesis temperatures (Fig. 3, region A), but further TEM and high-resolution TEM (HRTEM) investigations are required to determine fully the relationship between $Li_4Ti_5O_{12}$ and anatase formation.

Cyclic voltammetry measurements were performed to examine the electrochemical properties of the $Li_4Ti_5O_{12}$, and $Li_4Ti_5O_{12}$–TiO_2 powders during the charge–discharge process. Cyclic voltammograms of S-1, S-2 and S-3 electrodes at a scanning rate of 0.05 mV s^{-1} between 1.0 and 2.5 V are presented in Fig. 4. The cathodic peak located at around 1.5 V for all samples corresponds to the voltage platform of the discharge process, in which Li is intercalated into the spinel $Li_4Ti_5O_{12}$. The anodic peak located at 1.7 V for the S-1 electrode and 1.61 V for the S-2 and S-3 electrodes corresponds to the voltage platform of the charge process, in which Li is de-intercalated from the spinel $Li_7Ti_5O_{12}$. Similar results have been obtained by other workers [41–43]. As can be seen in Fig. 4, both S-2 and S-3 electrodes have a voltage plateaux at about 1.7 and at 2.0 V. These should correspond to the discharge and charge plateaux of anatase TiO_2 [41]. Only one oxidation/reduction peak is observed for the S-1 electrode, and no peak with characteristics of lithium ion insertion or extraction for anatase TiO_2 is observed. Since there are no other redox peaks in the cyclic voltammogram, the spinel $Li_4Ti_5O_{12}$ is evidently pure for the S-1 sample synthesized at very low temperature (300 °C), whereas with increasing temperature (400 and 500 °C), the $Li_4Ti_5O_{12}$ phase is partially transformed to anatase TiO_2, in accordance with the XRD results. The following Eqs. (1) and (2) explain lithium ion insertion into and extraction from spinel $Li_4Ti_5O_{12}$ and anatase TiO_2, respectively, during cycling processes. The process is associated with the redox reactions of Ti^{4+}/Ti^{3+} [44,6].

$$Li_4Ti_5O_{12} + xLi^+ + xe^- \leftrightarrow Li_{4+x}Ti_5O_{12} \quad (1)$$

$$TiO_2 + xLi^+ + xe^- \leftrightarrow Li_xTiO_2 \quad (2)$$

The amount of lithium insertion may depend on the crystalline nature and the microstructure of the material [45].

Simulated test cells were fabricated from electrodes S-1, S-2 and S-3 with metallic lithium to carry out galvanostatic charge–discharge tests (Fig. 5(a–c)). Initial discharge and charge curves at different current densities (0.2–5 C) in the range of 1.0–2.5 V were investigated. The respective initial discharge and charge capacities are:

185 and 132 mAh g^{-1} at 0.2 C, 69 and 62 mAh g^{-1} at 5 C for the S-1 electrode;
193 and 141 mAh g^{-1} at 0.2 C, 117 and 107 mAh g^{-1} at 5 C for the S-2 electrode;
169 and 152 mAh g^{-1} at 0.2 C, 63 and 54 mAh g^{-1} at 5 C for the S-3 electrode.

The discharge capacity decreases for all samples with increasing current density. Furthermore, some irreversible capacity loss is observed for all samples during the first cycle, which might

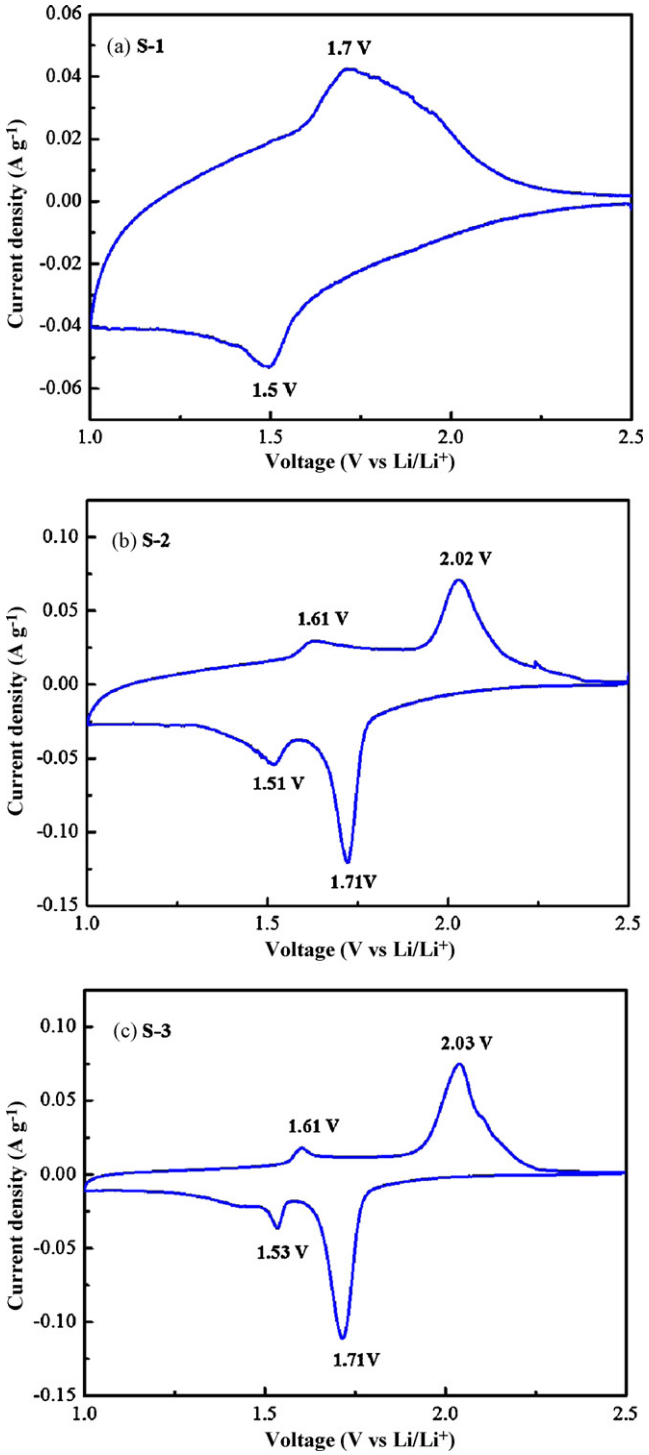

Fig. 4. Cyclic voltammograms of (a) S-1, (b) S-2 and (c) S-3 electrodes at a scan rate of 0.05 mV s^{-1} between 1.0 and 2.5 V.

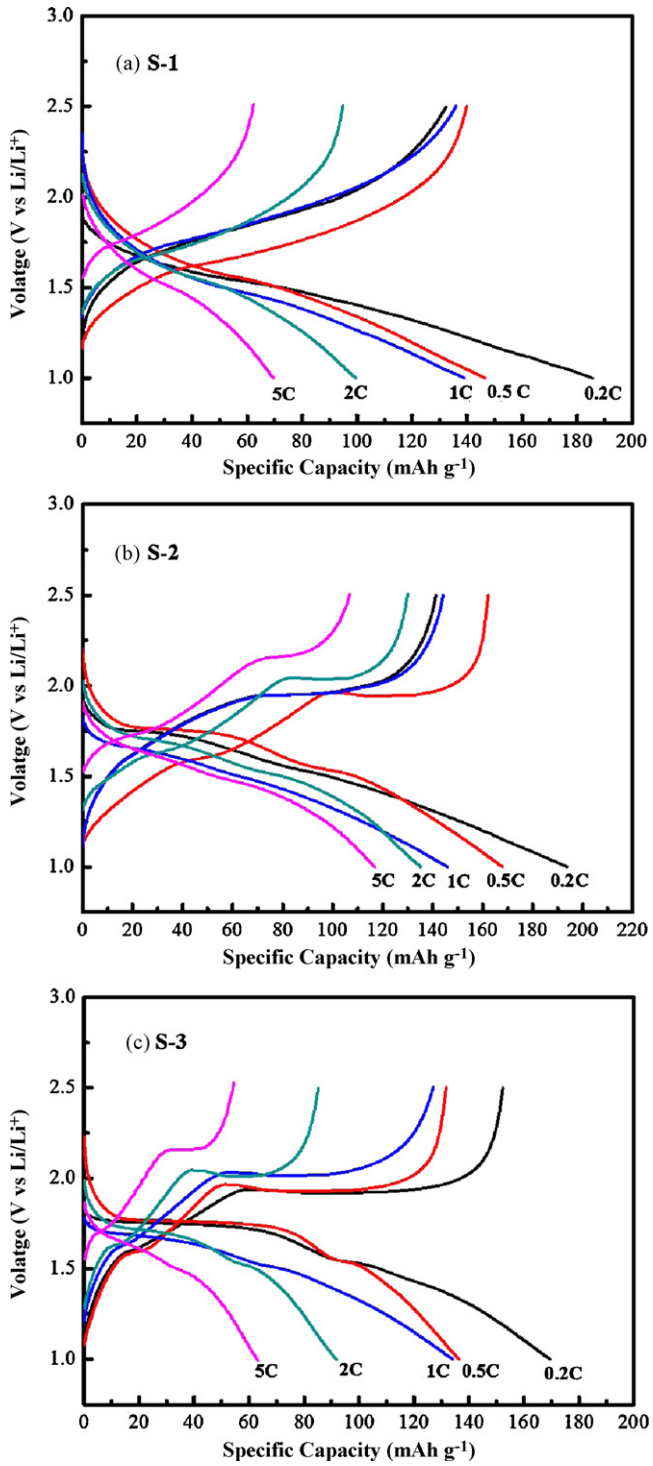

Fig. 5. Initial charge–discharge profiles of electrodes (a) S-1, (b) S-2 and (c) S-3 at different current densities from 0.2 to 5 C between 1.0 and 2.5 V vs. Li/Li^+.

be due to irreversible electrochemical decomposition of the electrolyte or an impurity phase on the $Li_4Ti_5O_{12}/TiO_2$ surface [48]. Sample S-1 prepared at low temperature (300 °C) delivers sloping charge–discharge curves instead of a flat plateau (Fig. 5(a)), which is consistent with material prepared by a thermohydro method at low temperature, as reported by Zhang et al. [46]. Differences in the charge–discharge profile are mostly correlated with crystal structure. As can be seen in Fig. 5(b) for S-2 and Fig. 5(c) for S-3, both the discharge and the charge curves have two flat voltage plateaux due to the formation of spinel $Li_4Ti_5O_{12}$ and anatase TiO_2. For the S-2 electrode, the discharge plateaux are observed at about 1.51 and 1.71 V, and the charge plateaux at about 1.61 and 2.02 V; and for the S-3 electrode, plateaux are observed at 1.53 and 1.71 V for discharge, and 1.61 and 2.03 V for charge, respectively. These data also agree with the cathodic and anodic peak potentials in the cyclic voltammograms.

The cycling behaviour, coulombic efficiency and rate capability of electrodes made from all samples are presented in Fig. 6. The cycling performance of the materials at 1 C (1 C = 175 mAh g^{-1})

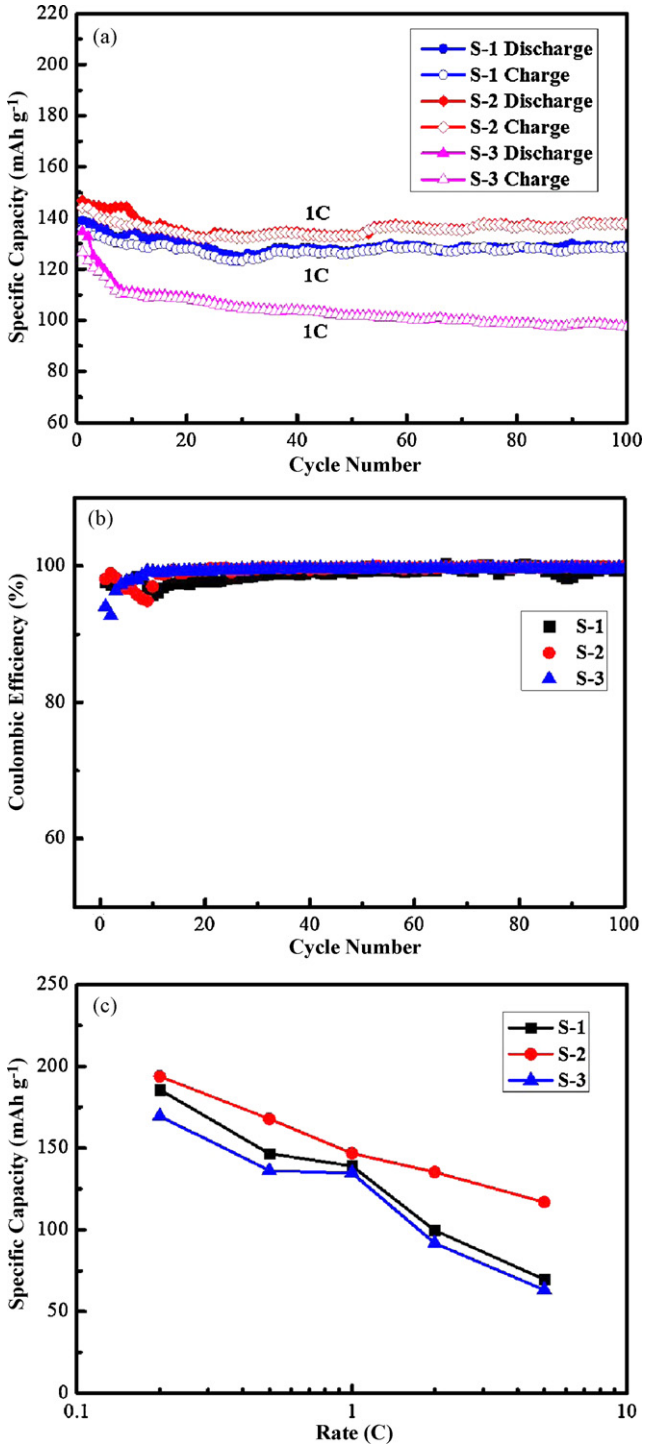

Fig. 6. (a) Cyclic performance at 1 C (1 C = 175 mAh g^{-1}); (b) coulombic efficiency measured at 1 C; (c) rate capability at different current densities from 0.2 to 5 C between 1.0 and 2.5 V vs. Li/Li^+ of S-1, S-2, and S-3 electrodes, respectively.

is shown in Fig. 6(a). It is seen that samples S-1, S-2 and S-3 have initial discharge/charge capacity of 139/135, 146/144 and 134/127 mAh g^{-1}, with an initial coulombic efficiency (Fig. 6(b)) of 97, 99, and 94%, respectively. This trend is maintained during long-term cycling. After 100 cycles, the discharge capacities are 129, 138 and 97 mAh g^{-1}, with capacity retention of 93, 95 and 72% of initial discharge capacity for S-1, S-2 and S-3 electrodes, respectively. The specific capacity and capacity retention follow the order of S-2 (400 °C) > S-1 (300 °C) > S-3 (500 °C), and coulombic efficiencies reached ~100% for all samples. The rate capability of the electrodes is shown as a function of the discharge/charge current rates from 0.2 to 5 C in Fig. 6(c). At a low rate of 0.2 C, the differences between the discharge capacities of the S-1, S-2 and S-3 electrodes are not so large. This is reasonable because Li^+ insertion/extraction is sufficient at this relatively low current rate. The difference between the lithium storage capacities of the S-1 and S-3 samples is still not significant with increasing discharge/charge current rate. The rate capability of the S-1 and S-3 electrodes is nearly same, whereas the high-rate capability of the S-2 electrode is much higher than that of the other two and shows very slow capacity fading with increasing current rate.

Why does the S-2 electrode show the best electrochemical performance? The reasons are still not fully understood, but the following possibilities could be considered. Nanostructured materials may allow the use of small transport lengths and small separation distances in almost the same way as in fluids. The materials synthesized here are obviously nanoparticles. The first difference to consider is the surface area. The S-1 sample has approximately four times the surface area of S-3, whereas S-2 has three times the surface area of S-3. A larger number of lithium insertion sites would be expected in the samples with higher surface area [49]. Thus, the S-1 sample should show the best electrochemical performance, but the reality is different. This is may be due to the presence of very dense agglomerations of ultra-fine particles (Fig. 2(c)) in the S-1 sample, which may hinder the insertion reaction, as intercalation can only occur with the outer atoms and is therefore limited. Besides this absorptive mechanism (insertion reaction), there is another adsorptive mechanism (reversible interfacial reaction), the capacity of which depends on the grain size in the first instance and, indeed, relies on the presence of nanoparticles. Different possibilities for interfacial reactions have been discussed in the literature: one is underpotential deposition [50], and a second is lithium storage by reaction with the grain boundary phase [47] in polycrystalline materials or by reaction with the liquid electrolyte at the solid|liquid interface [51,52]. In the present study, the second possible mechanism is considered, i.e., lithium storage by reaction with the grain boundary phase. Lithium storage in these samples relates to the presence of grain boundary interfaces between spinel $Li_4Ti_5O_{12}$ and anatase TiO_2. Heat treatment affects both the surface-to-volume ratio of the lithium titanate nanostructures and the total area of the interface between the anatase and the lithium titanate nanostructures, as indicated by the TEM observations (Fig. 2). The sample calcined at 300 °C is too dense, and the reversible interfacial reaction paths along the grain boundaries are too long. The sample calcined at 400 °C has a more open structure, with a very high area of interface between the anatase and the lithium titanate, while in the sample calcined at 500 °C, the grain boundary area per unit volume is lower to the extent that the electrochemical performance deteriorates.

4. Conclusions

Nanocrystalline $Li_4Ti_5O_{12}$–TiO_2 powder has been successfully synthesized by a simple basic molten salt process (BMSP) using an eutectic mixture of $LiNO_3$–$LiOH$–Li_2O_2. The results indicate that pure $Li_4Ti_5O_{12}$ phase with very small crystal size can be partially converted to anatase TiO_2 as a secondary phase with increasing heat-treatment temperature. In a sample prepared at 400 °C, a duplex crystallite size (fine (<10 nm), and coarse (>20 nm)) is observed. Electrochemical testing demonstrates that the sample synthesized at 400 °C has a stable high discharge–charge capacity with excellent rate capability. This finding strongly suggests that the synthesis process is very simple and convenient, and also requires only a low-treatment temperature. By virtue of this synthesis, nanostructured $Li_4Ti_5O_{12}$–TiO_2 has been demonstrated to be a highly promising anode material for Li-ion battery application.

Acknowledgements

The authors are grateful for funding from the Australian Research Council (ARC) under an ARC Centre of Excellence Program (CE0561616) and an ARC Discovery project (DP0987805). The authors also thank Dr. T. Silver for critical reading of the manuscript.

References

[1] Z. Yang, D. Choi, S. Kerisit, K.M. Rosso, D. Wang, J. Zhang, G. Graff, J. Liu, J. Power Sources 192 (2009) 588.
[2] S.-W. Woo, K. Dokko, K. Kanamuraa, Electrochim. Acta 53 (2007) 79.
[3] J.R. Owen, Chem. Soc. Rev. 26 (1997) 259.
[4] D. Aurbach, E. Zinigrad, Y. Cohen, H. Teller, Solid State Ionics 148 (2002) 405.
[5] J.M. Tarascon, M. Armand, Nature 414 (2001) 359.
[6] T. Yuan, R. Cai, K. Wang, R. Ran, S. Liu, Z. Shao, Ceram. Int. 35 (2009) 1757.
[7] H. Yu, X. Zhang, A.F. Jalbout, X. Yan, X. Pan, H. Xie, R. Wang, Electrochim. Acta 53 (2008) 4200.
[8] K.M. Colbow, J.R. Dahn, R.R. Haering, J. Power Sources 26 (1989) 397.
[9] E. Ferg, R.J. Gummow, A. de Kock, M.M. Thackeray, J. Electrochem. Soc. 141 (1994) L147.
[10] T. Ohzuku, A. Ueda, N. Yamamoto, J. Electrochem. Soc. 142 (1995) 1431.
[11] A. Deschanvers, B. Raveau, Z. Sekkal, Mater. Res. Bull. 6 (1971) 699.
[12] P.P. Prosini, R. Mancini, L. Petrucci, Solid State Ionics 144 (2001) 185.
[13] D. Liu, C. Ouyang, J. Shu, J. Jiang, Z. Wang, L. Chen, Phys. Status Solidi (b) 243 (2006) 1835.
[14] R.I. Eglitis, G. Borstel, Phys. Status Solidi (a) 202 (2005) R13.
[15] E.M. Sorensen, S.J. Barry, H. Jung, H.K. Jung, J.R. Rondinelli, Chem. Mater. 18 (2006) 482.
[16] H. Qiao, L. Xiao, L. Zhang, Electrochem. Commun. 10 (2008) 616.
[17] B.-L. He, B. Dong, H.-L. Li, Electrochem. Commun. 9 (2007) 425.
[18] H. Lindstrom, S. Sodergren, A. Solbrand, H. Rensmo, J. Hjelm, A. Hagfeldt, S.-E. Lindquist, J. Phys. Chem. B 101 (1997) 7717.
[19] M.V. Koudriachova, N.M. Harrison, S.W. de Leeuw, Phys. Rev. Lett. 86 (2001) 1275.
[20] S.I. Pyun, S.W. Kim, H.C. Shin, J. Power Sources 81/82 (1999) 248.
[21] G.G. Amatucci, F. Badway, A.D. Pasquier, T. Zheng, J. Electrochem. Soc. 148 (2001) A930.
[22] A.D. Pasquier, A. Laforgue, P. Simon, G.G. Amatucci, J.F. Fauvarque, J. Electrochem. Soc. 149 (2002) A302.
[23] A. Guerfi, S. Sevigny, M. Lagace, P. Hovington, K. Kinoshita, K. Zaghib, J. Power Sources 119–121 (2003) 88.
[24] S. Bach, J.P. Pereira-Ramos, N. Baffier, J. Power Sources 81/82 (1999) 273.
[25] C.M. Shen, X.G. Zhang, Y.K. Zhou, H. Li, Mater. Chem. Phys. 78 (2002) 437.
[26] Y.H. Rho, K. Kanamura, M. Fujisaki, J. Hamagami, S. Suda, T. Umegaki, Solid State Ionics 151 (2002) 151.
[27] K.N. Jung, S.I. Pyun, S.W. Kim, J. Power Sources 119–121 (2003) 637.
[28] J.H. Kim, S.T. Myung, Y.K. Sun, Electrochim. Acta 49 (2004) 219.
[29] L. Wen, Q. Lu, G.X. Xu, Electrochim. Acta 51 (2006) 4388.
[30] A. Lundblad, B. Bergman, Solid State Ionics 96 (1997) 173.
[31] Y. Gao, J.R. Dahn, J. Electrochem. Soc. 143 (1996) 100.
[32] T. Spitler, J. Prochazka, L. Kavan, M. Graetzel, F. Sugnaux, United States Patent, Patent No.: US 7,547,490 B2, 16 June 2009.
[33] E. Zhecheva, R. Stoyanova, M. Gorova, R. Alcantara, J. Morales, J.L. Tirado, Chem. Mater. 8 (1996) 1429.
[34] M. Okubo, E. Hosono, J.D. Kim, M. Enomoto, N. Kojima, T. Kudo, H.S. Zhou, I. Homma, J. Am. Chem. Soc. 129 (2007) 7444.
[35] J. Park, K. An, Y. Hwang, J.G. Park, H.-J. Noh, J.-Y. Kim, J.-H. Park, N.-M. Hwang, T. Hyeon, Nat. Mater. 3 (2004) 891.
[36] T. Kawamura, M. Makidera, S. Okada, K. Koga, N. Miura, J.I. Yamaki, J. Power Sources 146 (2005) 27.
[37] S.-W. Song, H. Fujita, M. Yoshimura, Adv. Mater. 14 (2002) 268.
[38] C.-H. Han, Y.S. Hong, C.M. Park, K. Kim, J. Power Sources 92 (2001) 95.
[39] H. Liang, X. Qiu, S. Zhang, Z. He, W. Zhu, L. Chen, Electrochem. Commun. 6 (2004) 505.
[40] L. Cheng, H.-J. Liu, J.-J. Zhang, H.-M. Xiong, Y.-Y. Xia, J. Electrochem. Soc. 153 (2006) A1472.
[41] J. Li, Y.-L. Jin, X.-G. Zhang, H. Yang, Solid State Ionics 178 (2007) 1590.

[42] Li. Cheng, H.-J. Liu, J.-J. Zhang, H.-M. Xiong, Y.-Y. Xia, J. Electrochem. Soc. 153 (8) (2006) A1472.
[43] Y.-J. Hao, Q.-Yu. Lai, D.-Q. Liu, Z.-Ui Xu, X.-Y. Ji, Mater. Chem. Phys. 94 (2005) 382.
[44] M. Venkateswarlu, C.H. Chen, J.S. Do, C.W. Lin, T.C. Chou, B.J. Hwang, J. Power Sources 146 (2005) 204.
[45] B.-L. He, B. Dong, H.-L. Li, Electrochem Commun. 9 (2007) 425.
[46] J. Li, Z. Tang, Z. Zhang, Electrochem. Commun. 7 (2005) 894.
[47] L.Y. Beaulieu, D. Larcher, R.A. Dunlap, J.R. Dahn, J. Electrochem. Soc. 147 (9) (2000) 3206.
[48] T. Yuan, K. Wang, R. Cai, R. Ran, Z. Shao, J. Alloys Compd. 477 (2009) 665.
[49] J.L. Allen, T.R. Jow, J. Wolfenstine, J. Power Sources 159 (2006) 1340.
[50] B.E. Conway, Electrochim. Acta 38 (1993) 1249.
[51] S. Grugeon, S. Laruelle, R. Herrera-Urbina, L. Dupont, P. Poizot, J.M. Tarascon, J. Electrochem. Soc. 148 (2001) A285.
[52] H. Li, G. Richter, J. Maier, Adv. Mater. 15 (2002) 735.